

University of Groningen

## Design and Evaluation of a Magnetic Rotablation Catheter for Arterial Stenosis

Heunis, Christoff M.; Behrendt, Kasper J.; Hekman, Edsko E.G.; Moers, Cyril; de Vries, Jean-Paul P.M.; Misra, Sarthak

*Published in:*  
IEEE/ASME Transactions on Mechatronics

*DOI:*  
[10.1109/TMECH.2021.3092608](https://doi.org/10.1109/TMECH.2021.3092608)

**IMPORTANT NOTE: You are advised to consult the publisher's version (publisher's PDF) if you wish to cite from it. Please check the document version below.**

*Document Version*  
Publisher's PDF, also known as Version of record

*Publication date:*  
2022

[Link to publication in University of Groningen/UMCG research database](#)

*Citation for published version (APA):*

Heunis, C. M., Behrendt, K. J., Hekman, E. E. G., Moers, C., de Vries, J-P. P. M., & Misra, S. (2022). Design and Evaluation of a Magnetic Rotablation Catheter for Arterial Stenosis. *IEEE/ASME Transactions on Mechatronics*, 27(3), 1761 - 1772. <https://doi.org/10.1109/TMECH.2021.3092608>

### Copyright

Other than for strictly personal use, it is not permitted to download or to forward/distribute the text or part of it without the consent of the author(s) and/or copyright holder(s), unless the work is under an open content license (like Creative Commons).




The publication may also be distributed here under the terms of Article 25fa of the Dutch Copyright Act, indicated by the "Taverne" license. More information can be found on the University of Groningen website: <https://www.rug.nl/library/open-access/self-archiving-pure/taverne-amendment>.

### Take-down policy

If you believe that this document breaches copyright please contact us providing details, and we will remove access to the work immediately and investigate your claim.

*Downloaded from the University of Groningen/UMCG research database (Pure): <http://www.rug.nl/research/portal>. For technical reasons the number of authors shown on this cover page is limited to 10 maximum.*

# Design and Evaluation of a Magnetic Rotablation Catheter for Arterial Stenosis

Christoff M. Heunis , Kasper J. Behrendt, Edsko E.G. Hekman , *Member, IEEE*, Cyril Moers, Jean-Paul P.M. de Vries, and Sarthak Misra , *Senior Member, IEEE*

**Abstract**—Arterial stenosis is a high-risk disease accompanied by large amounts of calcified deposits and plaques that develop inside the vasculature. These deposits should be reduced to improve blood flow. However, current methods used to reduce stenosis require externally controlled actuation systems resulting in limited workspace or patient risks. This results in an unexplored preference regarding the revascularization strategy for symptomatic artery stenosis. In this article, we propose a novel internally actuated solution: a magnetic spring-loaded rotablation catheter. The catheter is developed to achieve stenosis-debulking capabilities by actuating drill bits using two internal electromagnetic coils and a magnetic reciprocating spring-loaded shaft. The state-space model of the catheter is validated by comparing the simulation results of the magnetic fields of the internal coils with the experimental results of a fabricated prototype. Contact forces of the catheter tip are measured experimentally, resulting in a maximum axial force of 2.63 N and a torque of 5.69 mN-m. Finally, we present interventions in which the catheter is inserted to reach a vascular target site and demonstrate plaque-specific treatment using different detachable actuator bits. Calcified deposits are debulked and visualized via ultrasound imaging. The catheter can reduce a stenosis cross-sectional area by up to 35%, indicating the potential for the treatment of calcified lesions, which could prevent restenosis.

**Index Terms**—Actuators and sensors, magnetic systems, medical robotics, modeling and design, system integration.

Manuscript received January 18, 2021; revised March 31, 2021; accepted June 10, 2021. Date of publication June 28, 2021; date of current version June 16, 2022. Recommended by Technical Editor Z. Bi and Senior Editor W. J. Chris Zhang. This work was supported by the Netherlands Organization for Scientific Research (NWO – Innovational Research Incentives Scheme – VIDI: SAMURAI Project # 14855). (*Corresponding author: Christoff M. Heunis.*)

Christoff M. Heunis, Kasper J. Behrendt, and Edsko E.G. Hekman are with the Surgical Robotics Laboratory, Department of Biomechanical Engineering, University of Twente, 7500 AE Enschede, The Netherlands (e-mail: c.m.heunis@utwente.nl; k.j.behrendt@student.utwente.nl; e.e.g.hekman@utwente.nl).

Cyril Moers and Jean-Paul P.M. de Vries are with the Department of Surgery, University of Groningen and University Medical Center Groningen, 9713 GZ Groningen, The Netherlands (e-mail: c.moers@umcg.nl; j.p.p.m.de.vries@umcg.nl).

Sarthak Misra is with the Department of Biomedical Engineering, University of Groningen, and University Medical Center Groningen, 9713 GZ Groningen, The Netherlands (e-mail: s.misra@utwente.nl).

This article has supplementary material provided by the authors and color versions of one or more figures available at <https://doi.org/10.1109/TMECH.2021.3092608>.

Digital Object Identifier 10.1109/TMECH.2021.3092608

## I. INTRODUCTION

**A**THEROSCLEROSIS is a disease that is caused by a buildup of plaque in the arteries that deliver blood to vital organs and limbs [1]. Built-up plaque causes a narrowing of the arterial lumen, which in turn decreases the blood flow to the target organ or extremity. One of the prevalent disorders caused by atherosclerosis is called peripheral artery disease (PAD) [2], which affects arteries that supply blood to the legs and feet (Fig. 1). Diagnosing PAD is conventionally done by peripheral angiography. This involves using arterial catheters to inject a contrast medium into the peripheral arteries, along with intraoperative X-ray scans. The options of angioplasty or arterial bypass surgery depend largely on the severity of disease [3]. Subject to the amount of blockage in the arteries, clinicians may prescribe a percutaneous peripheral intervention in order to decrease or remove an obstruction, whereas the more extreme cases require complete peripheral arterial bypass grafting. Notwithstanding, initial treatments focus more on minimally invasive techniques, such as angioplasty or atherectomy, instead of bypass surgery [4].

Consequently, this focus has stimulated the development of percutaneous atherectomy devices for the mechanical removal of deposits [5], [6]. Such devices have also recently been advocated as a promising development in combination with drug-eluting balloon angioplasty [7]. A few commercially available devices have been introduced, including the TurboHawk and SilverHawk peripheral plaque excision systems (Medtronic, Dublin, Ireland) [8], the Turbo-series laser catheters (Spectranetics, Colorado, United States) [8], and the Diamondback 360 Peripheral Orbital Atherectomy System (Cardiovascular Systems, Minnesota, United States) [9]. Furthermore, Schmitt *et al.* demonstrated a rotational thrombectomy catheter, capable of removing acute and subacute occlusions in patients using the Rotarex catheter (Straub Medical, Wangs, Switzerland) [10]. However, these catheters contain high-frequency drilling devices with speeds of 30 000–120 000 r/min [11]. These high speeds could potentially cause microcavitation or inflect damage to the vessel walls due to heat production [12]. Besides, angiograms are employed as a visual aid to the clinicians, requiring X-ray imaging, and thus exposing patients and staff to an increased level of radiation.

This justifies the need for improved atherectomy actuators that can be steered precisely inside arteries. Based on this notion, magnetic manipulation strategies have been introduced to

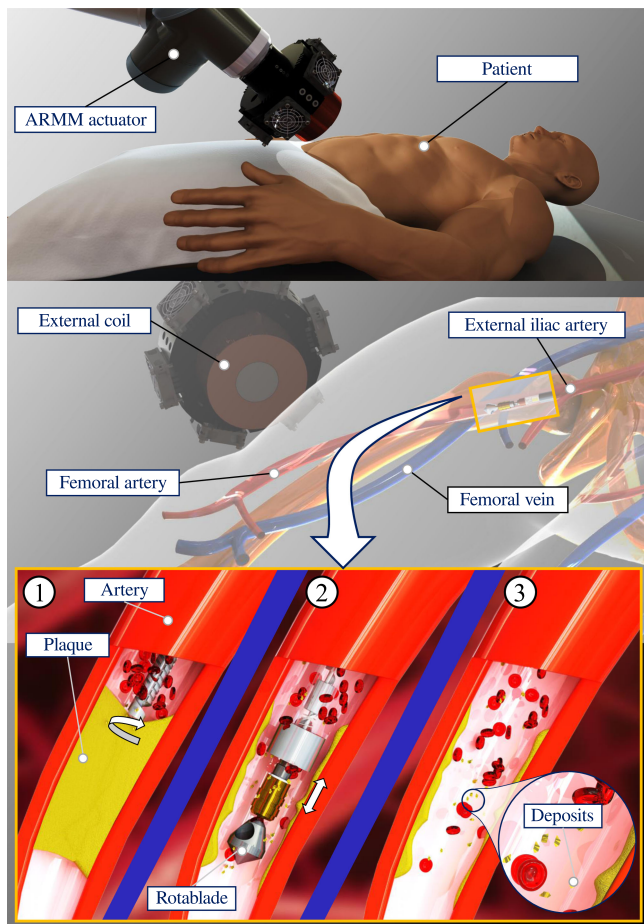


**Fig. 1.** Illustration of an atherectomy involving a tethered rotablation prototype: Stenosis occurs due to the buildup of fatty deposits on the inner arterial wall. The rotablation catheter can be utilized as an externally actuated intravascular drill using the Advanced Robotics for Magnetic Manipulation (ARMM) system. 1 The fatty deposits (plaque) are removed by advancing the catheter to the site, 2, and actuating the rotablation mechanism with a magnetic field. 3 Improved blood flow should then be established by the successful reduction of the deposits. This study aims to address 1 and 2.

treat PAD. One of the advantages of employing magnetic strategies is their suitability in restricted space, allowing for wireless control in an environment that is suitable for clinical applications [13]. Untethered (magnetic) actuators have shown some potential during *in vitro* experiments with artificial embolisms [14], [15]. Similarly, studies have demonstrated magnetic drilling actuators [16] and characterized their locomotion and drilling performance in vascular network-mimicking fluidic channels [17] and animal brain tissue [18]. Unfortunately, these actuators suffer from several drawbacks. First, the external magnetic fields are not strong enough to position them under high-pressured pulsatile flow and external excitation caused by the heartbeat. Furthermore, apart from Leclerc *et al.* [18], small untethered actuators do not have the potential to debulk stenoses effectively due to low actuation forces. Next, these novel actuators have yet to be demonstrated in a scenario where they can be inserted and removed using a catheter to avoid entrapment within calcified lesions. Based on these notions, there exists a need for

**TABLE I**  
MEDICAL CONSTRAINTS (C) AND DESIGN REQUIREMENTS (R) OF THE ROTABLATION CATHETER PROTOTYPE

Constraint (C) / Requirement (R)	Description	Motivation	
C1	Largest diameter ( $d_o$ ) of rotablation catheter should be less than artery diameter ( $d_a$ )	$d_o < 0.64(d_a)$ mm	Ensure proper flow lumen
C2	Minimum rotablator diameter ( $d_t$ ) should be at least 30% of artery diameter	$d_t \geq 0.3(d_a)$ mm	Debulk calcified deposits effectively
C3	Include power screw unit with non-locking screw motion	$41^\circ < \alpha < 49^\circ$	Ensure rotational and transluminal ablation
C4	Include detachable rotablation unit	Design of a catheter rotablator mount	Disposal of used rotablator
R1	Position catheter using external magnetic actuation	External ferromagnetic core	Maintain position under high-pressured pulsatile flow
R2	Actuate rotablation tip using internal magnetic actuation	Microcoil-magnet assembly	Ensure small surgical workspace
R3	Use optimal magnetic coil inner ( $r_c$ ) and outer ( $r_o$ ) radii ratio	$r_c/r_o \approx 0.53$	Ensure highest possible magnetic field strength
R4	Include spring-loaded actuator with spring force ( $F_k$ )	$F_k < F_M$ N	Increase magnetic thrust force ( $F_M$ )
R5	Resistive temperature increase ( $\Delta T_r$ ) should be low	$\Delta T_r < 7^\circ\text{C}$	Ensure safe operation inside artery

alternative actuation strategies that advance the state-of-the-art in the debulking of calcified deposits inside the arteries.

This article presents the design, fabrication, and evaluation of a magnetically actuated rotablation catheter. This catheter is aimed at debulking calcified deposits of arterial stenoses and occlusions. The prototype consists of two integrated electromagnetic coils and spring-loaded magnetized units that induce a rotation as a result of an internally generated magnetic field (as opposed to external actuation). This enables us to ensure the optimal size of both the catheter and the workspace.

This article is organized as follows. Section II describes the design and medical considerations of the prototype. In Section III, we formulate the mathematical expressions for the magnetic components and the kinematics, control, and thermodynamics of the catheter. The experimental setups for the force analyses and catheter insertion experiments, and results and discussion are presented in Section IV. Finally, Section V concludes this article.

## II. ROTABLATION CATHETER DESIGN

The design methods, modeling, and fabrication of the rotablation catheter are presented in this section. Several considerations are taken into account, including the medical and design constraints of the catheter (Table I), to translate the clinical needs into requirements.

### A. Medical Constraints

Generally, the first medical constraint of a catheter is the average diameter of the vasculature it is aimed to treat. PAD may occur within the peripheral arteries, with typical diameters ranging between 6–9 mm (femoral artery) and 8–12 mm (iliac artery) [19]. However, PAD has also been reported to be substantial within the infrarenal aorta, especially at the aortic bifurcation, which has reported diameters of 12–24 mm [20].

The maximum outer diameter of a catheter should allow for sufficient flow lumen diameter while not causing an excessive decrease in flow and potentially create stasis. Based on these estimated diameters, the prototype will be designed to be modular and scalable, such that it has a maximum catheter-to-vessel diameter ratio of 0.64 : 1 [21].

The second medical constraint is the degree of stenosis, conventionally defined as the narrowing (%) of the arterial inner diameter. Three degrees of stenosis for this study are chosen and categorized as Grade **I** (30%–49%) for eccentric lesions, Grade **II** (50%–99%) for concentric lesions, and a chronic total occlusion at Grade **III** ( $\approx 100\%$ ) [22]. These degrees allow us to design rotablation tips (rotablades) for debulking calcified deposits corresponding to the severity of the stenosis. The requirement for the minimum blade diameter ( $d_t$ ) is determined by the motivation to reduce a Grade **III** stenosis to Grade **II**.

The third and final medical constraint is to choose from the available techniques for performing atherectomy. Conventionally, these involve orbital, directional, transluminal, and rotational atherectomy techniques [10], [11], [23]. Both orbital and directional atherectomies require high rotational speeds, which are not attainable through magnetic actuation. However, rotational atherectomy is particularly effective in deposit removal [24]. This technique ensures that soft, healthy arterial tissues are deflected to avoid contact with the blade, while hard, calcified plaque is ablated. In our approach, this mechanism should be combined with a transluminal technique, in which the rotablation catheter is positioned coaxially in the artery.

## B. Design Requirements

In order to combine a rotational and transluminal atherectomy design, a power screw unit is required. The purpose of the power screw is to translate linear thrust to rotational motions. A nonlocking screw motion is obtained by ensuring a  $45^\circ \pm 4^\circ$  lead angle ( $\alpha$ ) [25]. The lead angle is calculated using

$$\alpha = \tan^{-1} \left( \frac{p}{\pi d_m} \right) \quad (1)$$

where  $p$  is the pitch size of the screw thread,  $\alpha$  is the pitch angle, and  $d_m$  is the mean diameter. The next requirement is that this integrated actuation unit should ablate plaque in both axial and tangential directions via magnetic actuation. Magnetic interaction occurs between a (ferro)-magnetic dipole ( $\boldsymbol{\mu} \in \mathbb{R}^3$ ) and the external field ( $\mathbf{B}(\mathbf{p}) \in \mathbb{R}^3$ ) at a point ( $\mathbf{p} \in \mathbb{R}^3$ ) in space [26]. In the presence of a magnetic field, this dipole experiences a wrench ( $\mathbf{W}_\mu \in \mathbb{R}^6$ ) comprising force ( $\mathbf{F}_\mu \in \mathbb{R}^3$ ) and torque ( $\mathbf{T}_\mu \in \mathbb{R}^3$ ) components, defined as

$$\mathbf{W}_\mu = \begin{bmatrix} \mathbf{F}_\mu \\ \mathbf{T}_\mu \end{bmatrix} = \begin{bmatrix} \nabla(\boldsymbol{\mu}^T \mathbf{B}(\mathbf{p})) \\ \boldsymbol{\mu} \times \mathbf{B}(\mathbf{p}) \end{bmatrix}. \quad (2)$$

The magnetic interaction between electromagnetic coils and permanent magnets should be employed to produce a drilling action resulting from a reciprocating shaft. The drilling action should be achieved by transforming linear motion (due to  $\mathbf{F}_\mu$

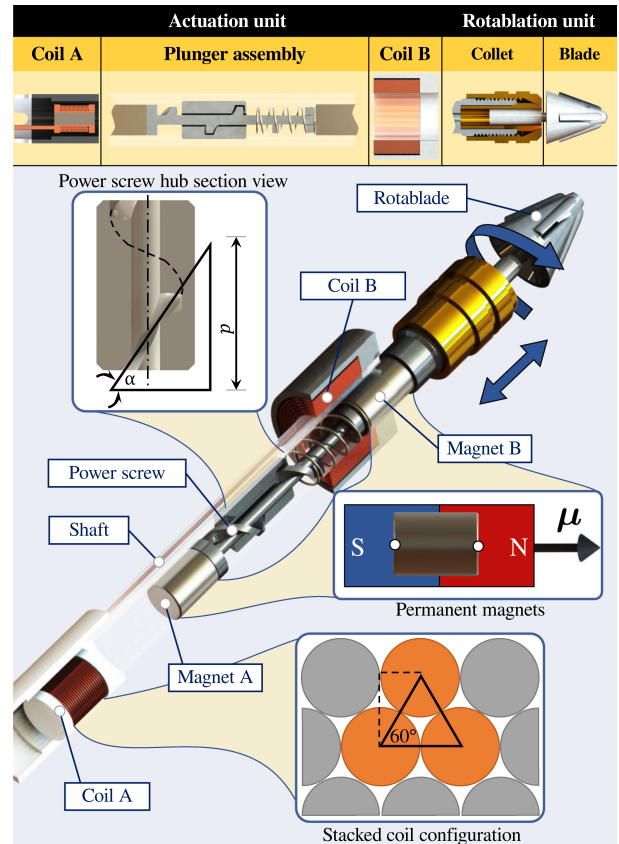


**Fig. 2.** Structure of the prototype which consists of two units—An actuation and rotablation unit. A partially sectioned view of the power screw hub (top-left inset) illustrates the relation between the pitch angle ( $\alpha$ ) and pitch ( $p$ ) of the thread. The blue arrow indicates the motions of the permanent magnets due to an alternating input current to the electromagnets (Coil A and Coil B). The inset (mid) shows the magnetic dipole moment ( $\mu$ ) of both magnets. The bottom inset shows the  $60^\circ$  stacked configuration of the copper wire.

exerting a magnetic repulsion force between the coil and the magnet) to a rotating motion (due to the power screw) (Fig. 2). The next design requirement is to ensure that sufficiently high magnetic forces are generated to actuate the rotablation catheter tip. For a maximum generated magnetic field, the ideal ratio between the core radius ( $r_c$ ) and outer radius ( $r_o$ ) of an electromagnetic coil is  $r_c/r_o \approx 0.53$ , assuming a stacked wire configuration of  $60^\circ$  [27]. This requirement is constrained by the resistive temperature of the copper wire, which influences the maximum current load rating per wire diameter size. According to the Food and Drug Administration (FDA), the maximum allowed temperature rise of instruments inside patient extremities is  $3^\circ\text{C}$ , although temperature increases of up to  $7^\circ\text{C}$  have been reported to result in negligible arterial damage [28]. In order to accommodate this constraint, the power screw should act as a spring-loaded actuator. The only requirement here is that the maximum compression force ( $F_k = k u_{\max}$ ) of the spring with stiffness ( $k \in \mathbb{R}$ ) at maximum compression ( $u_{\max} \in \mathbb{R}$ ) should be less than the maximum magnetic pulling force ( $F_M \in \mathbb{R}$ ). In addition, the spring should act as both a damper (during compression) and a thruster (during actuation).

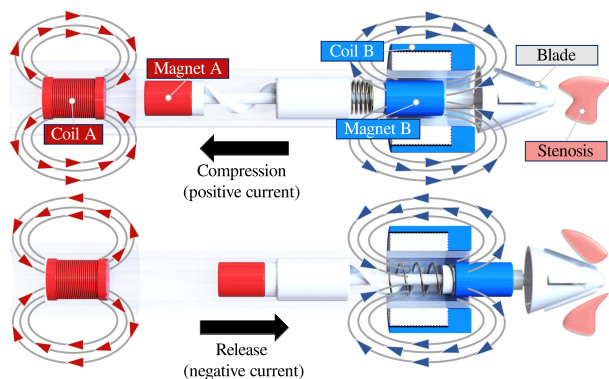


Fig. 3. Actuation principle for rotablation. Magnet A is actuated by Coil A (red), whereas Magnet B is actuated by Coil B (blue). During actuation, the coils are turned on (positive input current), causing the plunger assembly to retract and compress against the spring. Subsequently, the current is switched, which releases the plunger around the screw thread to engage the blade with stenotic material.

### C. Rotablation Catheter Structure and Components

With these constraints (Table I) and requirements in mind, we design components that comprise two main units (the actuation unit and the rotablation unit) that are embedded on a flexible catheter shaft (Fig. 2). The actuation unit consists of two copper-wound iron-cored coils and a plunger assembly. The latter contains two neodymium (NdFeB) cylindrical magnets, a power screw (and screw hub), and a compression spring. The cylindrical magnets are fixed to the power screw shaft. Their magnetic dipole moments are aligned with those of the electromagnetic coils. This alignment is important for both the balance of the screw and exerting the maximum magnetic force from the electromagnetic coils. Assuming that the magnetic moment of the cylindrical magnet is oriented similarly to the coil, the force between them would be in the same direction as the central coil axis. The screw hub is rigidly positioned inside a polyvinyl chloride (PVC) tube representing the catheter shaft. The spring-loaded power screw employs a trapezoidal single-start thread design. This is different from a regular bolt screw, as it results in a rapid motion that requires less actuation force, and induces lower friction against the thread surface.

The planned rotablation actuation principle is shown in Fig. 3. The electromagnetic coils are denoted as Coil A and Coil B and will be controlled simultaneously. The electromagnetic coils are wound to fit in (and on) the catheter shaft. The final function of the plunger assembly is supported by the aforementioned compression spring. Finally, the rotablation unit contains a detachable and disposable bit (rotablade). Three rotablades are designed based on conventional oval-shaped burrs with tapered edges [29]. During actuation, the aim is to increase the stroke distance and enlarge the lumen diameter with lateral blades. This technique is known as “differential cutting” whereby the burr abrades more rigid tissue that surrounds it and is deflected away from healthy vessel walls. The rotablade can be chosen before an atherectomy, based on the required clinical function for stenosis removal, and secured to the actuation unit via a 3-D-printed rotablade mount. This mount is designed similarly

TABLE II  
DESIGN SPECIFICATIONS OF THE MAGNETIC COMPONENTS

Specification (unit)	Variable	Value	
<b>Copper-wire microcoil</b>			
Outer diameter (mm)	$d_o$	Coil A: 7.74	Coil B: 12
Inner diameter (mm)	$d_i$	4	7
Length (mm)	$l_w$	8	10
Turns (-)	$n$	232	135
DC resistance ( $\Omega$ )	$R_{DC}$	2.24	5.13
Wire diameter (mm)	$w$	0.25	
Specific heat (assumed equal) ( $\frac{J}{kg \cdot K}$ )	$c$	400	
Density ( $\frac{kg}{m^3}$ )	$\rho_w$	8500	
Resistivity ( $\frac{\Omega}{m}$ )	$\alpha$	$1.7 \times 10^{-8}$	
<b>Soft Iron Grade FF-0000 core</b>			
Length (mm)	$l_c$	10	12
Outer diameter (mm)	$d_c$	4	14
Density ( $\frac{kg}{m^3}$ )	$\rho_c$	7000	
Flux density (T)	$B_m$	1.05	
<b>Neodymium (NdFeB) permanent magnets</b>			
Diameter (mm)	$d_p$	6	
Length (mm)	$l_p$	8	10
Residual magnetism (T)	$B_r$	1.42	1.29

to a collet, which allows rotablades to be secured firmly to the plunger assembly.

### III. PROTOTYPE MODELING AND ASSEMBLY

In this section, we characterize the electromagnetic coils in the actuation unit in order to develop a feed-forward controller. The design objective is to maximize the catheter tip forces by first optimizing the relative positions and geometry of both electromagnetic coils. In order to estimate these, the dynamics of the actuation unit are simulated in COMSOL Multiphysics (COMSOL Inc., Stockholm, Sweden). Furthermore, the stroke displacement and actuation cycle (defined as the time for a stroke displacement to be repeated) of the plunger assembly are estimated to determine the maximum screw pitch. This is followed by the assembly of the final prototype.

#### A. Characterization of the Electromagnetic Coils

A 7-mm (24 Fr) catheter shaft diameter defines the outer and inner diameters of Coil A and Coil B, respectively and the diameters of the permanent magnets (Table II). The electromagnetic coils are then fabricated as follows: Coil A is wound around a soft-iron core (Salomon’s Metalen B.V., Groningen, The Netherlands) and is positioned at the posterior end of the catheter shaft. Coil B is on the anterior end, though it is designed as a proportional solenoid actuator. The core of Coil B is thus covering the armature. In addition to propelling the rotablation unit forward, the inverted core-armature configuration enables positioning of the magnet external to the catheter shaft.

Next, we consider the maximum rated current that is suitable for the copper wire diameter. The ideal wire diameter for the current prototype coil sizes is 0.25 mm [30]. According to the American Wire Gauge (AWG) system, the recommended ampacity for this diameter at 30 °C ambient temperature is 0.86 A. However, since these coils would be submerged in

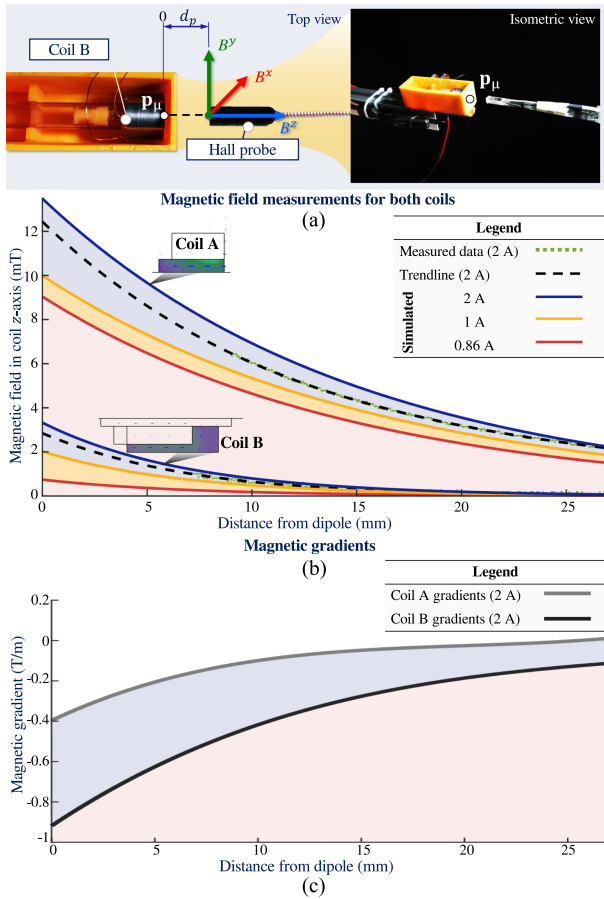


**Fig. 4.** Characterizing the electromagnetic coils (Coil A and Coil B) of the actuation unit. (a) Coil B is positioned in a container filled with water to compensate for resistive temperature rise. Each coil is measured separately using a continuous input current of 2 A. (b) A parametric sweep simulation is done for input currents of 0.86, 1, and 2 A and a distance of  $d_p = 0 - 26$  mm. The fields ( $B_z$ ) are then experimentally measured using a three-axis teslameter. The hall probe position is incremented along each coil symmetry axis ( $d_p = 8 - 26$  mm). Values below 8 mm are estimated indirectly by fitting fourth-order polynomial curves to the trendline of the measured data. (c) The magnetic gradients ( $\delta B_z / \delta d_p$ ) are estimated by differentiating the magnetic field value at each point in  $d_p$ .

water and subjected to fluid flow, we assume that they would not experience substantial damage with current activations of up to 2 A. Following defining the rated current, we can estimate the magnetic forces of the electromagnetic coils. For this purpose, we use COMSOL Multiphysics to simulate the magnetic field along the positive  $z$ -axis of both coils in a range of  $d_p = 0 - 26$  mm, where  $d_p = 0$  is on the point dipole ( $p_\mu$ ) of the coil. Simulations are done for current inputs of 0.86 A (recommended ampacity), 1 A, and 2 A (assumed ampacity). We compare the results of the last estimation (rated at 2 A) with magnetic field values that we experimentally measure using a calibrated three-axis teslameter (3MH3A-500MT Senis AG, Baar, Switzerland) (Fig. 4). Furthermore, we determine the magnetic field gradient ( $\delta B_z / \delta d_p$ ) indirectly by fitting fourth-order polynomial curves to the differentiated field values. Due to the coils being submerged in a container (hence obstructing the hall probe), the field curve is extrapolated for distances lower

than 8 mm. In the range for  $d_p$ , the current prototype delivers gradients of up to 0.91 T/m (Coil A) and 0.39 T/m (Coil B) and field ranges of 2.4–12.43 mT (Coil A) and 0.2–2.85 mT (Coil B). The average error and standard deviations between the observed and estimated fields are  $0.67 \pm 0.34$  mT for Coil A, and  $0.15 \pm 0.10$  mT for Coil B.

## B. Modeling the Plunger Assembly

In order to first determine the plunger actuation cycle, we consider a model of the plunger assembly. This model would allow us to simulate the unconstrained linear displacement of the plunger as a result of the coil magnetic forces. An unconstrained motion implies that the catheter tip is free to move without being constrained by the shaft. This allows us to observe the maximum displacement possible. The linear motion of the plunger assembly depends on the stroke distance ( $u$ )

$$m \frac{d^2 u}{dt^2} + c \frac{du}{dt} + ku - F_A - F_B + F_W = 0 \quad (3)$$

where  $m$  is the mass of the entire plunger assembly;  $k$  and  $c$  are the spring and damping coefficients, respectively;  $F_A$  and  $F_B$  are the magnetic thrust forces of Coil A and B, respectively; and  $F_W$  is the surface friction induced by the power-screw. The value for  $c$  is chosen as the critical damping coefficient ( $c = \sqrt{4mk}$ ) to zero amplitude resulting from possible oscillation. The total axial magnetic force ( $F_M = F_A + F_B$ ) acting on the plunger assembly is calculated within COMSOL Multiphysics using Maxwell stress tensor [31]. This is done by defining a fine moving mesh along the boundaries of the actuation unit. The axisymmetric geometry of the actuation unit is designed on a 2-D plane according to the model parameters shown in Table II. Both coils are modeled as multiturn induction coils, wherein the flux density ( $B$ ) is determined using the built-in COMSOL Multiphysics ac/dc module and Ampere's law

$$B = \phi n I \quad (4)$$

where  $n$  is the number of turns,  $\phi$  is the magnetic constant, and  $I$  is the input current. Both the cores and permanent magnet domains are modeled using separate built-in nodes and choosing their B-H curves as the constitutive relation. The 3-D model is obtained by a  $360^\circ$  revolution of the 2-D plane about the central axis situated within an air domain. The maximum displacement ( $u_{\max}$ ) of the assembly (and hence the tip) is influenced by the spring constant and distance between the coils and their respective magnets. From the 2-D distance-field curves of each coil shown in Fig. 4(b), we observe that the magnetic field for Coil B becomes significantly low at distances larger than 10 mm (77% reduction), whereas Coil A remains relatively high (around 6.92 mT). A parametric sweep is executed in COMSOL Multiphysics using these values as boundaries. The field distributions are visually inspected on a 2-D arrow plot to determine the areas at which their respective coils would influence magnets A and B at current inputs of 2 A. Hence, we analytically choose the fixed offset between the two coils. Given the knowledge of this offset and the rated current, the sweep parameters are chosen for the spring constant ( $k$ ) from a

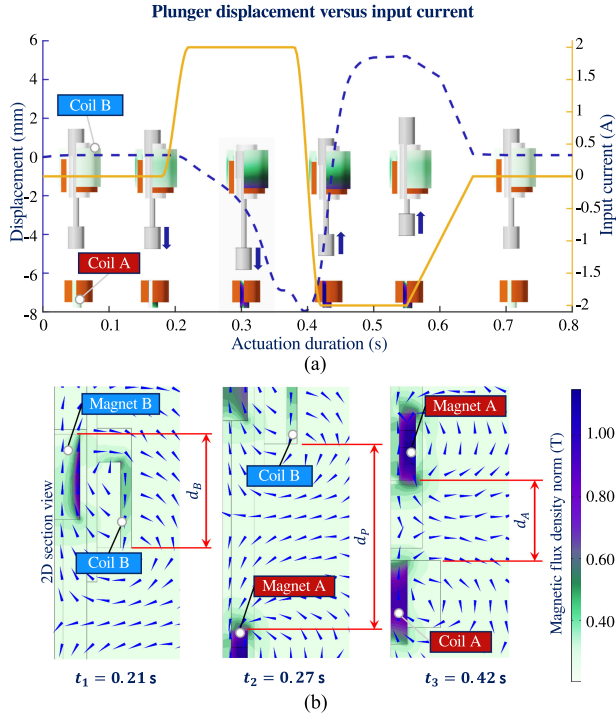


**Fig. 5.** (a) Estimated unconstrained displacement ( $\Delta p_u$ ) of the rotatable catheter tip for a single actuation cycle of 0.8 s. By supplying a current input of 2 A to both coils at 0.2 s, the combined electromagnetic forces on the permanent magnets cause a downward stroke of the tip for a distance of 8 mm. This is followed by switching the input current to  $-2$  A for both coils at 0.4 s, which propels the tip upwards. The total unconstrained displacement is 13.2 mm which is the chosen pitch size ( $p$ ) in (1) for the power screw. (b) The distances between the Coil B and Magnet B ( $d_B$ ), Coil B and Magnet A ( $d_P$ ), and Magnet A and Coil A ( $d_A$ ) are determined at the minimum and maximum stroke distance. Please refer to the accompanying [https://www.dropbox.com/s/dmr1e63bqg182ah/ARMM\\_Rotablation.mp4?dl=0](https://www.dropbox.com/s/dmr1e63bqg182ah/ARMM_Rotablation.mp4?dl=0) for further details.

range of commercially available miniature compression springs (Alcomex Verenfabriek B.V., Opmeer, The Netherlands). These spring dimensions are bounded by the free- and block spring lengths between Coil B and Magnet B, and the inner diameter of the catheter tube.

The subsequent steps are to calculate the stroke and dimensions of the power screw. Based on the parametric sweep results, the spring delivering the maximum stroke distance (13.2 mm) is chosen for the final assembly. This displacement is important since it allows us to determine the length and position of the power-screw and hub. Finally, a time-dependent study is executed and the tip motions are simulated using an input current of 2 A in an unconstrained actuation cycle [Fig. 5(a)]. As a result, (3) is solved, and the displacement ( $u$ ) of the assembly is obtained from the differential equations. The coil offsets are shown in Fig. 5(b) at the point of the minimum and maximum stroke distances.

### C. Final Prototype Assembly

Based on the calculated displacement ( $u$ ), the prototype is assembled. The design model and dimensions of the rotatable catheter components are shown in Fig. 6(a) and (b),

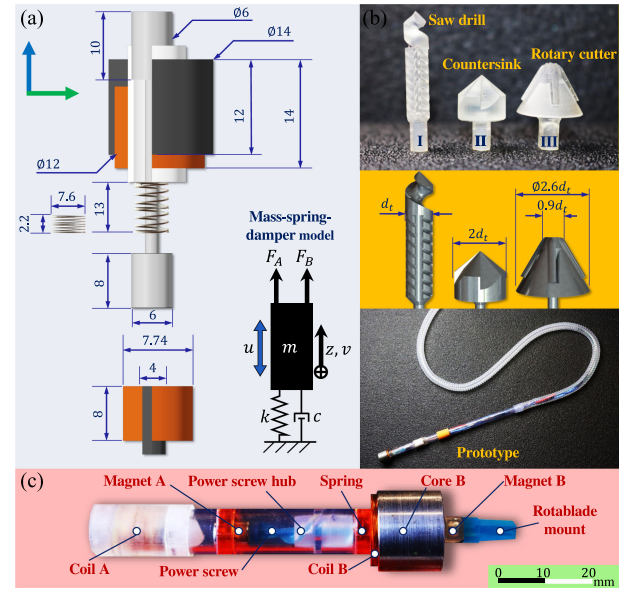


**Fig. 6.** (a) The design of the prototype, according to scale (all dimensions are in mm). The mass-spring-damper model is used to determine the forces that act on the rotablade shaft unit with mass ( $m$ ) during operation. The single degree-of-freedom motion takes electromagnetic forces due to Coil A ( $F_A$ ) and Coil B ( $F_B$ ) into account that influence the tip displacement ( $u$ ) and velocity ( $v$ ) in the positive  $z$ -direction. Finally, a damper and spring are added with respective coefficients ( $c$  and  $k$ ). (b) Three rotablades (top) are designed and tested with the rotatable catheter prototype (below). The minimum diameter ( $d_t$ ) is used to determine the ratios suitable to treat stenoses of Grades I, II, and III. (c) The final prototype.

whereas Fig. 6(c) shows the final prototype. The components are fabricated with ultraviolet resin (Photocentric, Peterborough, England) using 3-D stereolithography (SLA). First, the mean diameter ( $d_m$ ) of the power screw is selected as 3.6 mm to fit inside the catheter shaft. The pitch size is then determined by constraining the actuation to one single rotation only. Substituting  $p = u_{\max}$  in (1) delivers a pitch angle of  $\alpha = 49.4^\circ$ , which holds for constraint C3 (Table I). The screw hub is designed with a length of 12.5 mm and a free-running fit (h9-D9) tolerance, which is essential for translational accuracy and high-speed actuation. Next, the rotablades are designed. The ascending relation between the maximum diameters of the blades are defined as  $d_t$ ,  $2d_t$ , and  $2.6d_t$ , respectively [Fig. 6(b)]. Complying with constraint C2, for an inner aorta diameter of 24 mm,  $d_t$  is 8 mm.

Since the actuation cycle would differ in reality, we empirically tune the duration of the positive and negative input currents. A side view high-speed camera (MotionBLITZ Cube4, Mikrotron GmbH, Unterschleißheim, Germany) is used to obtain footage of the rotatable catheter tip displacement for three different actuation cycles (Fig. 7). It can be seen from this footage that, as opposed to the cycle shown in Fig. 5(a), the cycle that is on par with the simulated displacement, and thus ensuring the total stroke distance occurs, is 60 ms for each stroke. Using these cycles can also serve as a guideline to actuate the rotatable catheter with varying stroke distances.

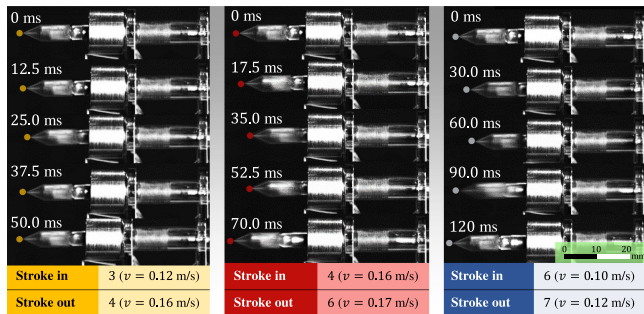


Fig. 7. High-speed (10 000 frames per second) footage of the prototype during actuation. The constrained displacements ( $\Delta p_c$ ) of the rotablation catheter tip are measured for actuation cycles of 50, 70, and 120 ms. The maximum expected stroke displacement of 13 mm occurs during an actuation cycle of 120 ms. Indicated stroke distances are in mm.

#### IV. PROTOTYPE TESTS

This section describes the experiments conducted for estimating the clinical feasibility of the prototype. The crucial factors to determine are the resistive heating of the electromagnetic coils inside a fluid, and the characterization of the actuation forces of the rotablation catheter tip. This is followed by an atherectomy procedure, where the rotablation catheter is used to debulk calcified deposits from three different types of artificial stenoses.

##### A. Resistive Heating of the Coils

At high input currents, the electromagnetic coils inevitably experience resistive heating—a factor which is important to consider during catheterizations. In order to test whether the rated current is suitable, we perform a heating experiment using a K-Type Thermocouple Module (Pmod TC1, Digilent Inc., Pullman, USA). Three thermocouples are connected to the rotablation catheter shaft containing both coils. The shaft is placed inside a water-filled container at room temperature (measured as  $20 \pm 1.2$  °C). The current supply to both coils are turned on while the sample time and measurements are recorded from each thermocouple. With a continuous current of 2 A, the average measured temperature increase at saturation is  $17 \pm 0.8$  °C in 20 min (Fig. 8). According to the limits mentioned above on temperature increase and as indicated in Fig. 8, we should ensure that the rotablation catheter is not operated continuously for durations that exceed 240 s.

##### B. Rotablation Catheter Tip Force and Torque Tests

Next, two force tests are conducted on the setups shown in Fig. 9. The axial test allows us to quantify the maximum thrust force ( $F_Z = F_M + F_k - F_W$ ) whereas, in the torque test, we calculate  $M_T = F_T r_T$ . Here,  $M_T$  is the torque determined by a tangential force ( $F_T$ ) at a single point of contact. A 3-D-printed, L-shaped drill bit with a torque distance arm ( $r_T$ ) is secured to the rotablation mount. By comparing the axial forces resulting from a nonthreaded shaft with those

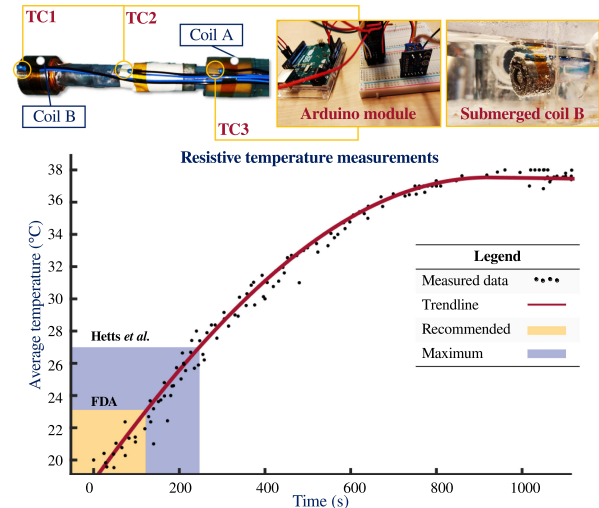


Fig. 8. Measuring the resistive temperature increase ( $\Delta T_r$ ) of the rotablation catheter via three thermocouples (TC\*, where \* = 1,2,3). Both coils are submerged in water at an initial temperature of 20 °C. An input current of 2 A is supplied to each coil for a duration of 20 min. The average measured temperature rise at steady state is  $17 \pm 0.8$  °C. Recommended and maximum reported temperature rises occur after approximately 125 and 240 s, respectively [28].

produced by the power screw, the friction ( $F_W$ ) induced by the power screw is determined experimentally. We also directly measure the effect of the compression force ( $F_k$ ) of the spring. In both experiments, contact forces are measured using a 3-axis force sensor (K3D40, Mesysteme AG, Henningsdorf, Germany).

Axial forces ( $F_Z$ ) are measured as follows. The rotablation catheter is fitted with a conical drill bit and rigidly attached to a steel frame [Fig. 9(a)]. The force sensor is then positioned coaxially, and the distance between the force sensor and tip is incremented in a range ( $u = 0 - 7$  mm). At each increment, the rotablation catheter is actuated for 20 cycles according to Fig. 5, and 3-D force data are recorded and averaged. Torques ( $M_T$ ) are measured similarly, however, the force sensor is fitted with a rigid beam [Fig. 9(b)]. The contact point of the bit is positioned at a stroke distance ( $u$ ) on this shaft, and 3-D contact forces ( $F_T$ ) are measured. The torque is then calculated for each increment.

The axial force-stroke curve is shown in Fig. 9(c). It can be seen that the presence of a spring substantially increases the axial force. Specifically, a force of 2.63 N occurs at the first increment after compression. Spring-loaded mechanical advantage plays a less significant actuation role after 7 mm. Fig. 9(d) shows the results of the torque tests. Again, the inclusion of the spring significantly increases the torque. The maximum torque is 5.69 mN-m and occurs at a 3-mm stroke. These force results imply that the rotablation catheter tip should be positioned as close as possible to debulk stenosis (within a 7-mm range). The resulting forces induced by the power screw thread are 0.07 N, which are relatively small (6.6%) compared to the maximum achievable thrust forces.



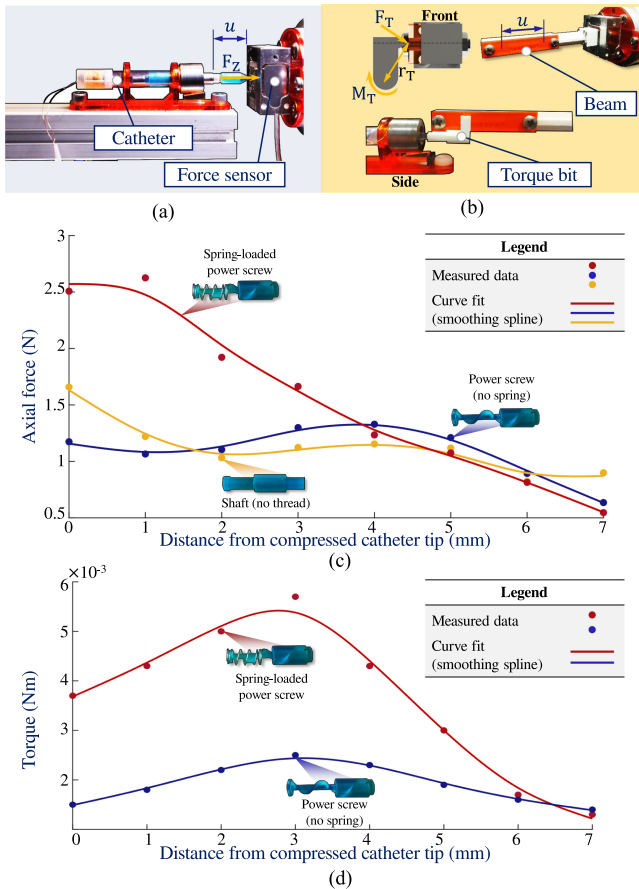


**Fig. 9.** Measured axial thrust forces and torques generated by the rotablation catheter. (a) The rotablation catheter is rigidly attached with its  $z$ -axis aligned with a 3-axis force sensor. Tip forces are measured in 1 mm increments for a stroke distance of  $u = 0 - 7$  mm. (b) A custom bit with a torque distance ( $r_T$ ) is designed for the torque measurements. The contact forces ( $F_T$ ) are measured along the same distance and increments, followed by calculating the torque ( $M_T$ ) at each increment. (c) Force-stroke graphs for the shaft, power screw, and spring-loaded power screw. (d) Torque versus stroke graphs for the screw and spring-loaded power screw. All measured data points are fitted with a smoothing spline.

### C. Phantom Fabrication

Next, we aim to demonstrate the working prototype in a fabricated phantom that simulates perfusion through the aorta. The phantom contains a silicone artery with an inner diameter similar to that of an aorta (24 mm), and contains a removable slot in which a segment of the (artificial) arterial stenosis can be placed. Pulsating fluid flow is simulated through the artery using a peristaltic pump (ISM 404, Ismatec, Wertheim, Germany). The properties of the artificial stenoses are chosen based on previous studies comparing their mechanical properties to gelatin-based phantoms [32], [33].

We prepare calcified arterial stenosis samples, with concentrations of gelatin and calcium carbonate dissolved in distilled water. By varying the concentration of gelatin and calcium carbonate, we test the feasibility of the prototype on both soft and hard plaques. The ratios for the soft plaque samples are 3% w/w chemical-grade gelatin added to distilled water (97% w/w) [17]. The addition of  $\text{CaCO}_3$  (6% w/w) results in a harder plaque [34].

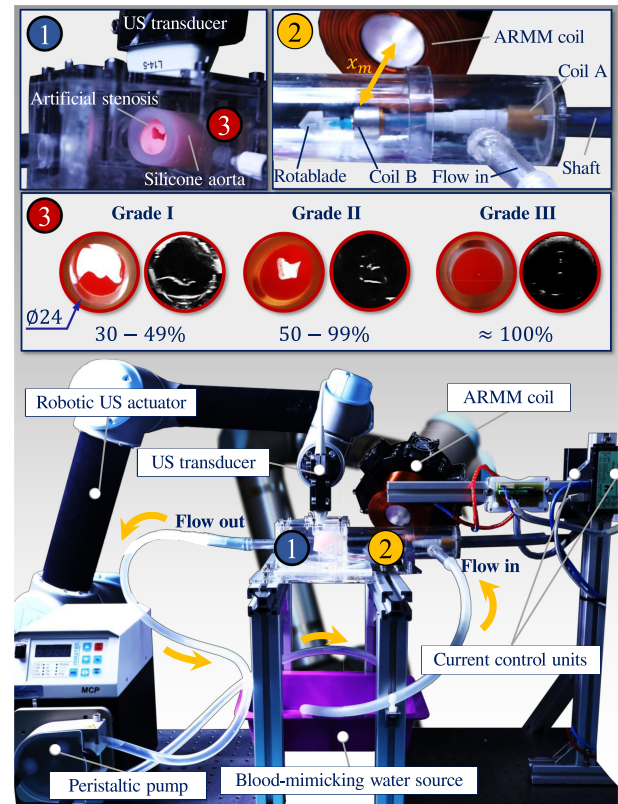


**Fig. 10.** Experimental setup for the atherectomy procedures. ① The ultrasound (US) transducer, (hard) artificial stenosis, and silicone aorta are shown inside the phantom. ② Close-up view of the rotablation catheter being advanced to the target point in the phantom at a distance ( $x_m$ ) from the external Advanced Robotics for Magnetic Manipulation (ARMM) coil [13]. ③ Camera (left) and US (right) images of the soft gelatine samples.

The soft and hard solutions are heated on a hot plate to  $70^\circ\text{C}$ . A preservative (0.05% w/w benzalkonium chloride) and a few drops of red acrylic dye are added. The solutions are then poured into three pairs of segments (30 mm long) of the silicone artery, with each pair containing a mold of the three different degrees of stenosis. The samples are then cooled down for 8 h at  $6^\circ\text{C}$ , after which the molds are removed. At this stage, the samples are ready and the performance of the rotablation catheter can be tested on each sample.

### D. Experimental Setup

The performance of the prototype is tested inside the Advanced Robotics for Magnetic Manipulation (ARMM) system [27]. The experimental setup is shown in Fig. 10. The actuation system comprises an external electromagnetic coil (ARMM coil) and a linear ultrasound (US) L14-5 transducer (SonixTouch Q+, BK Medical, Quickborn, Germany) that are both positioned by serial-link manipulators (UR10 and UR5, Universal Robots, Odense, Denmark). The current supply to the ARMM coil is controlled using a XenusPlus EtherCAT Master (XEL-230-40, Copley Controls, Canton, USA) amplifier, whereas the current supply to each electromagnetic coil is controlled and amplified using an EtherCAT servo drive (iPOS4808 BX-CAT, Technosoft

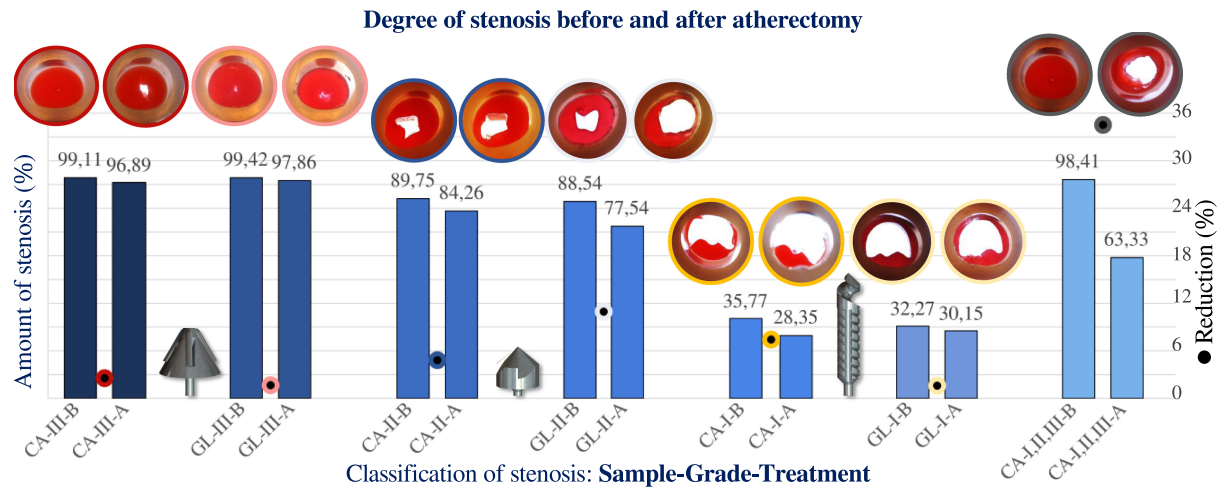


**Fig. 11.** Results of the atherectomy procedures. Each ultrasound (US) slice is analyzed in Matlab R2020a (Mathworks, Natick, USA) by tracing a region of interest (stenosis boundary) and creating a binary mask of the visible lumen surface. The amount of stenosis (%) is then calculated by taking the area of the lumen and subtracting that from the cross-sectional area of the artificial aorta. The amount of stenosis (%) is indicated above each column. Each circle between a column pair indicates the amount of stenosis reduction (%). The column pairs represent each procedure and indicate the classification of stenosis as the calcification type (CA = hard CaCO<sub>3</sub> sample, GL = soft gelatine sample), the grade of the stenosis (I, II, and III) treated in one procedure, and the treatment phase (B = before, A = after) of a procedure.

S.A., Neuchtel, Switzerland). Both drives and the amplifier are connected to the ARMM workstation (Intel Xeon processor E5-1650 v4, 6 GHz) running Ubuntu 18.04 (Kernel 4.4.236) via an EtherCAT network (control rate 500 Hz). The phantom is secured between the manipulators, and the first segment of the artificial arterial stenosis is placed within the phantom. A pulsatile flow is set to 2.9 L/min, which is a realistic flow rate for the aorta [35]. Finally, the ARMM coil is aligned at a distance ( $x_m \in \mathbb{R}^+$ ) from the dipole (on the core) to the face of the coil, in order to stabilize the rotablation catheter tip.

### E. Atherectomy Procedures

The three pairs of soft and hard artificial stenoses samples are inserted in the phantom on separate occasions, with each representing an individual scenario (Fig. 10.3). This is followed by the preparation of the rotablation catheter containing the rotablate for the particular sample. Hence, the saw drill is used to debulk deposits from Grade I soft and hard samples, the countersink blade for Grade II, and the rotary cutter for Grade III. The US transducer is employed to acquire 2-D US images before and after each procedure (Fig. 10.1). During image acquisition, the UR5 positions the US transducer above the site of stenosis on a silicone membrane. The position of this membrane is known *a priori*. We also investigate the total reduction of an additional Grade III hard sample using all three rotablades intraprocedurally. This results in a total of seven different procedures. During each procedure, the rotablation catheter tip is manually inserted into the phantom aorta. Once the rotablation catheter tip is in the vicinity of the lumen of the stenosis, the external ARMM coil is turned on. Next, atherectomy commences for 20 cycles (Fig. 7). For consistency between the procedures, only six instances of these cycles occur. Subsequently, a US image is taken of the stenosis, and the rotablation catheter is removed and prepared for the next sample. The results of these procedures are summarized

in Fig. 11. The most efficient rotablate for the soft sample (GL) stenosis is shown to be the countersunk blade (11.0% reduction), whereas hard samples (CA) were treated more efficiently with the saw drill (7.4% reduction) for one atherectomy procedure. The final procedure has resulted in a reduction of the stenosis cross-sectional area by up to 35%. Though there is no clear consensus in literature, clinicians generally consider a 30–35% reduction as significant, assuming that there is an additional PTA (and additional stenting) of the stenotic segment. The measurement of a pressure gradient should in theory provide more precise information (5–10 mmHg) [36]. This reduction is also on par with that of conventional devices, such as the Jetstream Navitus (Boston Scientific, Marlborough, USA), which is reported to reduce up to 30% stenosis [29].<sup>1</sup>

### F. Clinical Feasibility

In this study, certain clinical aspects of the catheter, including the feasibility of the actuation principle and the prototype size, have been presented. Based on the type of occlusion, the rotablate may be exchanged before the insertion or intraprocedurally. The progressive stenosis which leads to occlusion may in some cases result in several layers of additional thrombi. For example, during an early evolution of an eventual acute occlusion of eccentric stenosis, an asymmetric narrowing of the artery occurs. In this case, a directional atherectomy can be performed with the rotary cutter. The blade can be forced sideways against the plaque using the ARMM coil, and the larger cuttings can then be collected inside the catheter. During a more progressive narrowing of a long-standing concentric stenosis, or a chronic total occlusion, both areas with soft plaques, and with fibrosis (hard plaques) will form. Here, the saw drill and

<sup>1</sup>Please refer to the accompanying [https://www.dropbox.com/s/dmr1e63bqg182ah/ARMM\\_Rotablation.mp4?dl=0](https://www.dropbox.com/s/dmr1e63bqg182ah/ARMM_Rotablation.mp4?dl=0) video that demonstrates these procedures.

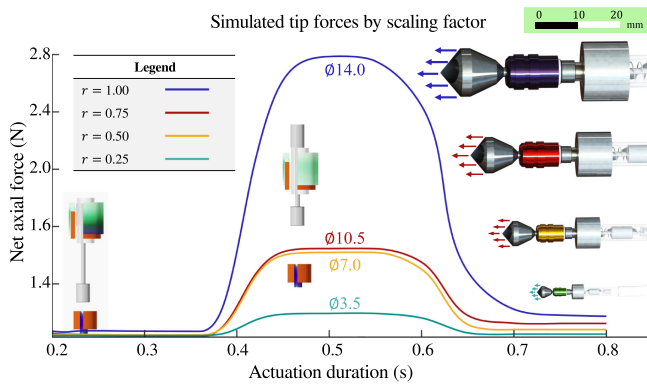


**Fig. 12.** Effect of scaling the prototype down several factors of the original size. The graph shows the simulated net forces acting on the catheter tip during an actuation cycle presented in Fig. 5. The current prototype (ratio 1.00) is shown in blue, followed by sizes pertaining to ratios ( $r$ ) of 0.75 in red, ( $d_o = 10.5$  mm), 0.50 in yellow ( $d_o = 7$  mm), and 0.25 in cyan ( $d_o = 3.5$  mm) of the original scale.

countersink blade are suitable to use. Notwithstanding, it is important to stress that the current prototype can pass and debulk stenosis, and that certain limitations should be addressed in order to improve the design in terms of the complete removal of deposits. First, the current prototype is only safe to use for uninterrupted durations lower than 240 s at a continuous rated current of 2 A. However, each actuation cycle occurred in short bursts as shown in the accompanying<sup>2</sup> video, followed by a 10-s pause after each actuation to maintain a low heat rise, resulting in 74.4 s duration per intervention. Any heat produced by the coils should be monitored over longer interventional durations, for instance, by fitting the catheter with Fiber Bragg Grating temperature sensors at the distal section [37].

Second, the maximum catheter diameter and rigid length ( $14 \times 76$  mm) indicate that the current prototype would be suitable for direct surgical access and atherectomies within the infrarenal aorta. This size is comparable to the 14-mm diameter Impella (Abiomed, Tokyo, Japan) heart-assistive catheters, which can be inserted percutaneously [38]. In order to insert the current prototype via the iliac artery (10 mm), it would have to be fabricated at half the current size, such that its maximum diameter is 7 mm. This scaled diameter would also be on par with conventional atherectomy catheter diameters (6.35 – 7.00 mm) [39]. Fig. 12 illustrates the simulated net axial forces acting on the plunger in miniaturized versions of this prototype. The maximum force of each scaled prototype is compared to forces reported by Zheng *et al.* (0.22 N) [11] and Leclerc *et al.* (0.06 N) [18]. The actuation forces of all scaled catheters is expected to be higher. It is, however, possible to scale the catheter magnetic elements down to a size that is applicable in smaller diameter arteries without losing actuation power, as demonstrated in our previous work [30]. In this work, we have found that the distribution of a scaled magnetic field remains constant, whereas the gradients decrease by the same factor or ratio ( $r$ ). This notion indicates that the miniaturization of systems

for magnetic actuation is a valid way of increasing the magnetic gradients available for actuating components with smaller coils.

The contribution of this prototype is that both its actuation mechanism and means of control represent a departure from conventional actuation and design. The majority of commercial devices utilize tendon-driven actuators to be steered or internally actuated [39]. This actuation deforms the entire catheter inner-structure in order to generate motion, resulting in complex dynamics. As the catheter is inserted deeper into the vasculature, the clinician gradually loses the ability to control the tip motions due to the interaction of the compliant environment with the catheter body. With our prototype, manual control is unnecessary, as the entire actuation is located on the distal segment. According to an extensive review by Ali *et al.* none of the existing commercially available systems is known to be using the technique of internal magnetic actuation due to its complexity [40]. However, our design approach is simple and intuitive and the prototype demonstrated the effective debulking stenoses of varying stiffness under pulsatile simulated blood flow. Moreover, current screw-inspired prototypes containing magnetic elements all require a rotating magnetic field in order to function. These rotating fields are induced by external Helmholtz coils that reduce the available workspace to small sizes that are not suitable for any extremity of a patient, such as a leg. This catheter does not require Helmholtz coils to be actuated and, instead, can be stabilized at a single position using the ARMM system.

## V. CONCLUSION

This study presented the design and evaluation of a novel magnetically actuated rotablation catheter aimed at treating arterial stenosis and occlusions. The rotablation catheter is actuated by internal electromagnetic coils and spring-loaded permanent magnets that are embedded on its distal end, allowing for both rotational and transluminal atherectomies. We have described the modeling of both the coils and magnetic components to realize an atherectomy prototype. Finally, we have demonstrated the feasibility of this prototype using a feed-forward controller inside a phantom arterial model. The rotablation catheter tip can exert a maximum axial force of 2.63 N and a torque of 5.69 mN-m. It can reduce a stenosis cross-sectional area by up to 35%, indicating the potential for the treatment of calcified lesions, which could prevent restenosis. Further improvements and design considerations are necessary to fabricate a clinic-ready rotablation catheter.

In our future work, we plan to utilize the current model and miniaturize the prototype such that it is suitable for the treatment of stenosis occurring in smaller arteries. Furthermore, the complete debulking of atherosclerotic plaque is essential, since any peripheral micro- and macroemboli emerging from the drilling process is considered a potential risk to the limb and patient. Thus, the presented procedure will be extended to include aspiration of debulked material into the rotablation catheter head, or fragmentation of material into pieces small enough to be aspirated into a suction chamber. To alleviate additional risks, like dissection or localized rupture of the artery,

<sup>2</sup>[Online]. Available: [https://www.dropbox.com/s/dmr1e63bqg182ah/ARMM\\_Rotablation.mp4?dl=0](https://www.dropbox.com/s/dmr1e63bqg182ah/ARMM_Rotablation.mp4?dl=0)

the catheter design will include a covered stent. The design will also be optimized to investigate the dynamic behavior through an analytical model. Finally, a feedback control strategy will be utilized to allow for the full 3-D control of the distal end of the rotablation catheter shaft by utilizing the external magnetic field of the ARMM system coil under real-time US imaging guidance. This would allow for the debulking of stenoses on preoperatively specified points inside the arterial wall, allowing for a more efficient atherectomy procedure.

## REFERENCES

- [1] Vaidya *et al.*, "Screen or not to screen for peripheral arterial disease: Guidance from a decision model," *BMC Public Health*, vol. 14, no. 1, 2014, Art. no. 89.
- [2] Lovell *et al.*, "Peripheral arterial disease: Lack of awareness in Canada," *Can. J. Cardiol.*, vol. 25, no. 1, pp. 39–45, 2009.
- [3] A. D. Michaels and K. Chatterjee, "Angioplasty versus bypass surgery for coronary artery disease," *Circulation*, vol. 106, no. 23, pp. e 187–e190, 2002.
- [4] A. Diamantopoulos and K. Katsanos, "Atherectomy of the femoropopliteal artery: A systematic review and meta-analysis of randomized controlled trials," *J. Cardiovasc. Surg.*, vol. 55, no. 5, pp. 655–665, 2014.
- [5] K. Rosenfield and K. N. Garratt, "The "appropriateness" of AUC for peripheral arterial disease: The story continues," *Catheterization Cardiovasc. Interv.*, vol. 90, no. 4, pp. 648–649, 2017.
- [6] D. G. Kokkinidis and E. J. Armstrong, "Emerging and future therapeutic options for femoropopliteal and infrapopliteal endovascular intervention," *Interventional Cardiol. Clin.*, vol. 6, no. 2, pp. 279–295, 2017.
- [7] Bhatia *et al.*, "Drug-eluting balloon angioplasty for in-stent restenosis following carotid artery stent placement," *J. Neuroimaging*, vol. 30, no. 3, pp. 267–275, 2020.
- [8] D. Mittleider and E. Russell, "Peripheral atherectomy: Applications and techniques," *Techn. Vasc. Interventional Radiol.*, vol. 19, no. 2, pp. 123–135, 2016.
- [9] J. H. Rundback and K. C. Herman, "Optimal use of atherectomy in critical limb ischemia," *Techn. Vasc. Interventional Radiol.*, vol. 17, no. 3, pp. 211–218, 2014.
- [10] Lee *et al.*, "A study of tool pattern design for calcified-atherosclerotic-plaque removal robot," in *Proc. IEEE RAS/EMBS Int. Conf. Biomed. Robot. Biomechanics*, Tokyo, Japan, 2010, pp. 582–587.
- [11] Zheng *et al.*, "Experimental investigation of the grinding wheel dynamics in atherectomy," in *Proc. 43rd North Amer. Manuf. Res. Conf.*, Charlotte, NC, USA, 2015.
- [12] Reisman *et al.*, "Analysis of heat generation during rotational atherectomy using different operational techniques," *Catheterization Cardiovasc. Diagnosis*, vol. 44, Art. no. 453.
- [13] Heunis *et al.*, "The ARMM system-autonomous steering of magnetically-actuated catheters: Towards endovascular applications," *Robot. Automat. Lett.*, vol. 5, no. 2, pp. 704–711, 2020.
- [14] Mahdy *et al.*, "Characterization of helical propulsion inside in vitro and ex vivo models of a rabbit aorta," in *Proc. IEEE Int. Conf. Eng. Med. Biol. Soc.*, Berlin, Germany, 2019, pp. 5283–5286.
- [15] Zhang *et al.*, "Artificial bacterial flagella: Fabrication and magnetic control," *Appl. Phys. Lett.*, vol. 94, no. 6, 200, Art. no. 064107.
- [16] Lee *et al.*, "Effective locomotion and precise unclogging motion of an untethered flexible-legged magnetic robot for vascular diseases," *IEEE Trans. Ind. Electron.*, vol. 65, no. 2, pp. 1388–1397, Feb. 2018.
- [17] Lee *et al.*, "Fabrication and characterization of a magnetic drilling actuator for navigation in a three-dimensional phantom vascular network," *Sci. Rep.*, vol. 8, no. 1, 2018, Art. no. 3691.
- [18] Leclerc *et al.*, "Magnetic hammer actuation for tissue penetration using a millirobot," *Robot. Automat. Lett.*, vol. 3, 2018, Art. no. 403.
- [19] H. Stiegler and R. Brandl, "Periphere arterielle Verschlusskrankheit: Stellenwert der Sonografie," *Ultraschall der Medizin-Eur. J. Ultrasound*, vol. 30, no. 4, pp. 334–374, 2009.
- [20] Osnabrugge *et al.*, "Aortic stenosis in the elderly," *J. Amer. College Cardiol.*, vol. 62, no. 11, pp. 1002–1012, 2013.
- [21] T. P. Nifong and T. J. McDevitt, "The effect of catheter to vein ratio on blood flow rates in a simulated model of peripherally inserted central venous catheters," *Chest*, vol. 140, no. 1, pp. 48–53, 2011.
- [22] Lorbeer *et al.*, "Reference values of vessel diameters, stenosis prevalence, and arterial variations of the lower limb arteries in a male population sample using contrast-enhanced MR angiography," *PLoS one*, vol. 13, no. 6, 2018, Art. no. e0197559.
- [23] Schmitt *et al.*, "A new rotational thrombectomy catheter: System design and first clinical experiences," *CardioVascular Interventional Radiol.*, vol. 22, pp. 504–509, 1999.
- [24] Cavusoglu *et al.*, "Current status of rotational atherectomy," *Catheterization Cardiovasc. Interv.*, vol. 62, no. 4, 2004, Art. no. 485.
- [25] V. Bhandari, *Design of Machine Elements*. 3rd ed. New York, NY, USA: McGraw-Hill, 2010.
- [26] A. J. Petruska and J. J. Abbott, "Optimal permanent-magnet geometries for dipole field approximation," *IEEE Trans. Magn.*, vol. 49, no. 2, pp. 811–819, Feb. 2013.
- [27] Sikorski *et al.*, "The ARMM system: An optimized mobile electromagnetic coil for non-linear actuation of flexible surgical instruments," *IEEE Trans. Magn.*, vol. 55, no. 9, pp. 1–9, Sep. 2019.
- [28] Hetts *et al.*, "Endovascular catheter for magnetic navigation under MR imaging guidance: Evaluation of safety in vivo at 1.5 T," *Amer. J. Neuro-radiol.*, vol. 34, no. 11, pp. 2083–2091, 2013.
- [29] N. I. Akkus and A. Abdulbaki, *Rotational Atherectomy in Peripheral Arterial Interventions*. Cham, Switzerland: Springer, 2018, pp. 1377–1388.
- [30] Sikorski *et al.*, "MILIMAC: Flexible catheter with miniaturized electromagnets as a small-footprint system for microbotic tasks," *Robot. Automat. Lett.*, vol. 5, no. 4, pp. 5260–5267, 2020.
- [31] Lubin *et al.*, "Simple analytical expressions for the force and torque of axial magnetic couplings," *IEEE Trans. Energy Convers.*, vol. 27, no. 2, pp. 536–546, Jun. 2012.
- [32] Huang *et al.*, "Assessing the viscoelastic properties of thrombus using a solid-sphere-based instantaneous force approach," *Ultrasound Med. Biol.*, vol. 37, no. 10, pp. 1722–1733, 2011.
- [33] Huang *et al.*, "Estimating the viscoelastic modulus of a thrombus using an ultrasonic shear-wave approach," *Med. Phys.*, vol. 40, no. 4, 2013, Art. no. 042901.
- [34] Jeon *et al.*, "Drug-enhanced unclogging motions of a double helical magnetic micromachine for occlusive vascular diseases," *IEEE Trans. Magn.*, vol. 50, no. 11, pp. 1–4, Nov. 2014.
- [35] Taylor *et al.*, "In vivo quantification of blood flow and wall shear stress in the human abdominal aorta during lower limb exercise," *Ann. Biomed. Eng.*, vol. 30, pp. 402–408, 2002.
- [36] L. Baert and M. Cowling, *Vascular Interventional Radiology: Angioplasty, Stenting, Thrombolysis and Thrombectomy, Ser. Medical Radiology*. Springer, Berlin, Heidelberg, 2006.
- [37] Rao *et al.*, "In-fiber bragg-grating temperature sensor system for medical applications," *J. Lightw. Technol.*, vol. 15, no. 5, pp. 779–785, 1997.
- [38] Burzotta *et al.*, "Impella: Pumps overview and access site management," *Minerva Cardioangiologica*, vol. 66, no. 5, pp. 606–611, 2018.
- [39] Hu *et al.*, "Steerable catheters for minimally invasive surgery: A review and future directions," *Comput. Assist. Surg.*, vol. 23, no. 1, pp. 21–41, 2018.
- [40] Ali *et al.*, "Steerable catheters in cardiology: Classifying steerability and assessing future challenges," *IEEE Trans. Biomed. Eng.*, vol. 63, no. 4, pp. 679–693, Apr. 2016.



**Christoff M. Heunis** (Student Member, IEEE) received the M.Sc. degree in mechatronic engineering from the University of Stellenbosch, Stellenbosch, South Africa, in 2016. He is currently working toward the Ph.D. degree in biomedical engineering with the Surgical Robotics Laboratory, University of Twente, Enschede, The Netherlands.

His research interests include the design of clinical equipment for the treatment of endovascular, cardiovascular, and oncological disorders.



**Kasper Behrendt** received the B.Sc. and M.Sc. degrees in biomedical engineering from the University of Twente, Enschede, The Netherlands, in May 2015 and September 2020, respectively.

His research at the Surgical Robotics Laboratory focused on the design of magnetically actuated atherectomy catheters.



**Edsko Hekman** received the B.Sc. degree in science and engineering from Calvin College, Grand Rapids, MI, USA, in 1981, and the M.Sc. degree in mechanical engineering from the Delft University of Technology, Delft, The Netherlands, in 1986.

After six years of developing equipment for medical research with the Radboud University, Nijmegen, The Netherlands, he joined the Research and Teaching Staff of the University of Twente, Enschede, The Netherlands. His main

research interests include the development of prosthetic, orthotic, and robotic devices for restoration of gait.



**Cyril Moers** received the Ph.D. degree from Rijksuniversiteit Groningen, Groningen, The Netherlands, in 2011.

He is currently a Transplant Surgeon and an Assistant Professor with the University Medical Center, Groningen. His recent research interests include interventions before or during organ preservation to better conserve organ quality and to quantify the impact that donor characteristics have on post-transplant outcome.

Prof. Moers was a recipient of an ERC Start-

ing Grant in 2019.



**Jean-Paul de Vries** received the Doctor in Medicine (MD) degree from the Vrije Universiteit Amsterdam, Amsterdam, The Netherlands, in 2001.

He is currently a Professor in Surgery with the University of Groningen and with the Department of Surgery, University Medical Center Groningen (UMCG). He is currently a Vascular Surgeon and Head of the Department of Surgery of the University Medical Center, Groningen, Groningen, The Netherlands. He is

also a Professor in surgery.

Prof. dr Vries is one of the founders of the Dutch Endovascular Alliance (DEALL), a multicentre Dutch research platform to perform dedicated (endo)vascular research. He is in the frontiers of innovative research focusing on optimizing imaging pre and postendovascular aneurysm repair, and development of noninvasive tissue perfusion techniques in peripheral arterial disease.



**Sarthak Misra** received the master's degree in mechanical engineering from McGill University, Montreal, QC, Canada, and the Ph.D. degree in mechanical engineering from the Johns Hopkins University, Baltimore, MD, USA.

He was a Robotics Analyst on the International Space Station Program with the Canadian Space Agency. He is currently a Full Professor with the University of Twente, Enschede, The Netherlands, and also affiliated with the University Medical Center Groningen, Groningen, The

Netherlands. He directs the Surgical Robotics Laboratory. His research interests include dynamics and control of micro/macro medical robotic systems.

Dr. Misra was the recipient of the ERC Starting, Consolidator, and Proof-of-Concept grants, and the NWO VENI and VIDI awards.